

# Kibble-Zurek scaling of the superfluid-supersolid transition in an elongated dipolar gas

Wyatt Kirkby,<sup>1,2</sup> Hayder Salman,<sup>3,4</sup> Thomas Gasenzer,<sup>1,5</sup> and Lauriane Chomaz<sup>2</sup>

<sup>1</sup>*Kirchhoff-Institut für Physik, Universität Heidelberg, Im Neuenheimer Feld 227, 69120 Heidelberg, Germany*

<sup>2</sup>*Physikalisches Institut, Universität Heidelberg, Im Neuenheimer Feld 226, 69120 Heidelberg, Germany*

<sup>3</sup>*School of Engineering, Mathematics, and Physics, University of East Anglia, Norwich Research Park, Norwich, NR4 7TJ, UK*

<sup>4</sup>*Centre for Photonics and Quantum Science, University of East Anglia, Norwich Research Park, Norwich, NR4 7TJ, UK*

<sup>5</sup>*Institut für Theoretische Physik, Universität Heidelberg, Philosophenweg 16, 69120 Heidelberg, Germany*

(Dated: November 28, 2024)

We simulate interaction quenches crossing from a superfluid to a supersolid state in a dipolar quantum gas of  $^{164}\text{Dy}$  atoms, trapped in an elongated tube with periodic boundary conditions, via the extended Gross-Pitaevskii equation. A freeze-out time is observed through a delay in supersolid formation, in comparison to the adiabatic case. We compute the density-density correlations at the freeze-out time and extract the frozen correlation length for the solid order. An analysis of the freeze-out time and correlation length versus the interaction quench rate allows us to extract universal exponents corresponding to the relaxation time and correlation length based on predictions of the Kibble-Zurek mechanism. Over several orders of magnitude, clear power-law scaling is observed for both, the freeze-out time and the correlation length, and the corresponding exponents are compatible with predictions based on the excitation spectrum calculated via Bogoliubov theory. Defects due to independent local breaking of translational symmetry, contributing to globally incommensurate supersolid order, are identified, and their number at the freeze-out time is found to also scale as a power law. Our results support the hypothesis of a continuous transition whose universality class remains to be determined but appears to differ from that of the (1+1)D XY model.

## I. INTRODUCTION

Spontaneous breaking of translational symmetry in a superfluid can result in an exotic phase of matter that maintains phase coherence while exhibiting periodic crystalline order: a supersolid [1–6]. Supersolids have been realized in ultracold quantum gases using spin-orbit-coupled systems [7, 8], and with strongly-magnetic dipolar atoms [9–11]. In the latter, the transition to a solid phase can be achieved either starting from a thermal gas and quenching the temperature [11–13], or starting from a superfluid and changing the interparticle interaction strength [9–11]. Furthermore, depending on the system parameters and geometry, the quantum phase transition from superfluid to supersolid has been found to be either continuous or discontinuous [14–20], however the exact critical behavior and the corresponding universality classes of these transitions have yet to be determined.

When tuning a control parameter  $\lambda$  towards its critical value  $\lambda_c$  at a continuous phase transition, characteristic scales diverge following universal power laws, defining the critical behavior at the phase transition and being independent of the microscopic details. Precisely, the correlation length  $\xi$  and relaxation time  $\tau$  diverge as  $\xi(\lambda) \sim |\lambda - \lambda_c|^{-\nu}$  and  $\tau(\lambda) \sim \xi^z \sim |\lambda - \lambda_c|^{-\nu z}$ , respectively, with  $\nu$  and  $z$  the critical exponents determined by the universality class of the transition [21–23], see Fig. 1 (a) and (b).

The theory of the Kibble-Zurek mechanism (KZM) [24–27] provides a framework for understanding symmetry breaking in a dynamical setting. It predicts that critical slowing down and the divergence of characteristic length and time scales prevent the system from preserving an instantaneous parametric equilibrium state

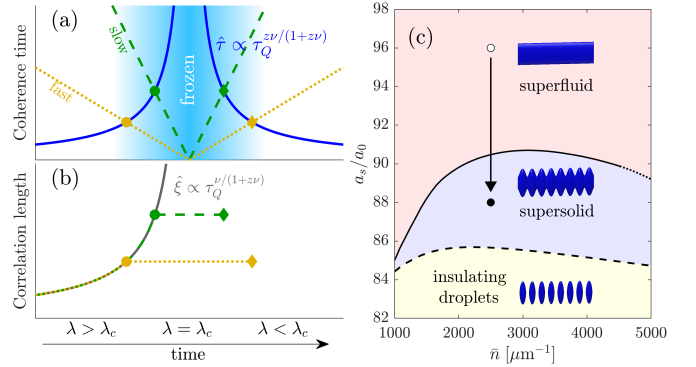


FIG. 1. KZM in quenches across the superfluid-supersolid transition. Panel (a) depicts the typical KZM schematic. The coherence time  $\tau$  (blue curve) diverges at the critical point. Two quench ramps linear in time  $t$  (slow: green-dashed, fast: yellow-dotted) of a control parameter are indicated. The freeze-out time  $\hat{\tau}$  occurs when  $|t|$  crosses  $\tau$ . Panel (b) depicts the diverging correlation length  $\xi$  (grey solid curve), which becomes frozen at  $\hat{\xi}$  as depicted here for the two ramps of panel (a). Panel (c) shows the phase diagram for the elongated dipolar system, with a continuous (solid line) or discontinuous (dotted line) transition from superfluid to supersolid phases, and a crossover from supersolid to insulating droplet (dashed line). Sample isodensity surfaces for each phase are shown. The start (empty circle) and end points (filled circle) for the quenches considered in this paper are indicated.

in quenches across continuous phase transitions. More specifically, in a quench of the control parameter  $\lambda$ , such as  $\lambda - \lambda_c \propto t/\tau_Q$ , the relaxation time  $\tau(t)$  rapidly increases and surpasses the time left to the transition at time  $t = -\hat{\tau} = -\tau(\hat{\tau})$ , so-called freezing-out time. For  $t > -\hat{\tau}$ , adiabaticity is broken, the system becomes

frozen, and fluctuations present remain embedded in the system until it unfreezes, which similarly occurs at a certain time after crossing the critical point, namely for  $t > \hat{\tau}$ . During the freeze-out period and as adiabaticity is lost, domains with distinct local order roughly of size  $\hat{\xi} = \xi(\hat{\tau})$  persist.

Based on the equilibrium scaling laws above, the freeze-out time and domain size for a linear quench of the order parameter at a constant rate  $\tau_Q$  scale as,

$$\hat{\tau} \propto \tau_Q^{z\nu/(1+z\nu)} \equiv \tau_Q^{\zeta_{\text{KZ}}} \quad \text{and} \quad \hat{\xi} \propto \tau_Q^{\nu/(1+z\nu)} \equiv \tau_Q^{\nu_{\text{KZ}}}, \quad (1)$$

respectively, see Fig. 1 (a) and (b). Higher quench rates lead to adiabaticity breaking at lower values of  $\hat{\tau}$  and  $\hat{\xi}$ , therefore corresponding to a shorter delay in domain formation and with smaller domains. The boundaries of these domains can be identified as defects, corresponding to sudden changes in the value of the order parameter in space, and separating independent causally-disconnected regions where the symmetry is independently broken. By studying the scaling of the freeze-out time, domain size, or remaining defects, one can extract critical scaling exponents of the underlying transition and thereby probe the transition universality class.

The KZM has been successfully applied to a wide range of systems [27–29]. This is in particular true for quantum gases where it has been studied both theoretically [30–43], and experimentally, via temperature quenches [44–57] and in quantum phase transitions [50, 58–64]. The transition to supersolid states offers a new context, where the KZM could be induced and its study may yield new insights into the nature of the underlying transitions.

In this paper, we study the KZM in the context of a continuous quantum phase transition from a superfluid to a one-dimensional supersolid in an elongated tube at a fixed density by tuning the  $s$ -wave scattering length  $a_s$ , see Fig. 1 (c). We cross the transition at a finite rate, and examine the scalings of the characteristic scales with the quench rate. In Section II, we present the equations of motion for the dipolar gas, illustrate how the ground state phase diagram is calculated, and present details of our dynamical simulations. Sections III D–III C presents our observations for power-law scalings of the freeze-out time, domain size, and defect densities, respectively, along with the corresponding scaling exponents. In Sec. III D, based on these KZM scalings, we extract the critical exponents  $\nu$  and  $z$  of the superfluid-to-supersolid transition and comment on its universality class.

## II. MODEL

### A. Equations of motion

To simulate the dipolar gas, we begin with the extended Gross-Pitaevskii equation (eGPE),

$$i\hbar \frac{\partial \Psi(\mathbf{r}, t)}{\partial t} = \left[ -\frac{\hbar^2 \nabla^2}{2m} + V(\mathbf{r}) + g|\Psi(\mathbf{r}, t)|^2 + \gamma_{\text{QF}} |\Psi(\mathbf{r}, t)|^3 + \int d^3 r' U_{\text{dd}}(\mathbf{r} - \mathbf{r}') |\Psi(\mathbf{r}', t)|^2 \right] \Psi(\mathbf{r}, t), \quad (2)$$

for atomic species with mass  $m$  and contact interaction strength  $g = 4\pi\hbar^2 a_s/m$  for an  $s$ -wave scattering length  $a_s$ . We assume the system is harmonically trapped along two directions via  $V(\mathbf{r}) = \frac{1}{2}m(\omega_y^2 y^2 + \omega_z^2 z^2)$  while the  $x$ -direction is untrapped. The dipole-dipole interaction (DDI) is given by  $U_{\text{dd}}(\mathbf{r}) = \mu_0 \mu_m^2 (1 - 3\cos^2 \theta)/(4\pi|\mathbf{r}|^3)$  where  $\theta$  is the angle between  $\mathbf{r}$  and the  $z$  axis, along which the dipoles are polarized. Each atom has a magnetic moment  $\mu_m$ , and  $\mu_0$  is the vacuum permeability. The supersolid phase is protected from collapse [65–67] by the beyond-mean field quantum fluctuations term proportional to  $\gamma_{\text{QF}} = \frac{32}{3}g\sqrt{a_s^3/\pi}\mathcal{Q}_5(\epsilon_{\text{dd}})$  [68], with  $\mathcal{Q}_5(\epsilon) = \text{Re}\{\int_0^1 du [1 + (3u^2 - 1)\epsilon]^{5/2}\}$ , where  $\text{Re}\{\cdot\}$  denotes the real part,  $\epsilon_{\text{dd}} = a_{\text{dd}}/a_s$  and  $a_{\text{dd}} = \mu_0 \mu_m^2/(12\pi\hbar^2)$ . The wavefunction is normalized to the total particle number  $N = \int d^3 r |\Psi(\mathbf{r})|^2$ .

We use a reduced 3D model introduced in Refs. [15, 69, 70], which assumes that the wavefunction  $\Psi(\mathbf{r})$  is separable,

$$\Psi(\mathbf{r}) = \varphi(y, z)\psi(x, t), \quad (3)$$

with radial wavefunction,

$$\varphi(y, z) = \frac{1}{\ell\sqrt{\pi}} \exp\left[-\frac{\eta y^2 + z^2/\eta}{2\ell^2}\right], \quad (4)$$

where  $\ell$  and  $\eta$  are variational parameters corresponding to the  $1/e$  condensate width and ellipticity (due to magnetostriction), respectively, obtained via minimization of the eGPE in imaginary time. The reduced eGPE then reads

$$i\hbar \frac{\partial \psi(x, t)}{\partial t} = \left[ -\frac{\hbar^2}{2m} \frac{\partial^2}{\partial x^2} + \mathcal{E}_\perp + \frac{g}{2\pi\ell^2} |\psi(x, t)|^2 + \frac{2\gamma_{\text{QF}}}{5\pi^{3/2}\ell^3} |\psi(x, t)|^3 + \int dx' U^{1\text{D}}(x - x') |\psi(x', t)|^2 \right] \psi(x, t), \quad (5)$$

where  $\mathcal{E}_\perp = \hbar^2(\eta + 1/\eta)/(4m\ell^2) + m\ell^2(\omega_y^2/\eta + \eta\omega_z^2)/4$ , and where we have defined the effective quasi-1D DDI  $U^{1\text{D}}(x - x')$ , which, for dipoles polarized along the  $z$  axis,

has the Fourier representation,  $\tilde{U}^{1D}(k) = \mu_0 \mu_m^2 [4 - 2\eta - 3\sqrt{\eta} k^2 \ell^2 e^{\sqrt{\eta} k^2 \ell^2 / 2} \text{Ei}(-\sqrt{\eta} k^2 \ell^2 / 2)] / [12\pi \ell^2 (1 + \eta)]$ , where  $\text{Ei}(k)$  is the exponential integral, and  $k$  is the conjugate momentum to the  $x$  coordinate. We will focus on an elongated gas of  $^{164}\text{Dy}$ , with  $\mu_m = 9.93 \mu_B$  in terms of the Bohr magneton  $\mu_B$ , in an elongated tube with trapping frequencies  $\{\omega_y, \omega_z\} = 2\pi \times \{150, 150\}$  Hz.

## B. Ground states

Prior to performing any quenches, we consider the ground state properties of the system. In order to determine the ground state of the system, and therefore the phase diagram, we perform an imaginary-time evolution of the reduced eGPE given in Eq. (5). We apply a split-step Fourier algorithm with an adaptive time step. For the ground state and dynamic simulations (next section), a spatial grid of approximately  $0.04 \mu\text{m}$  is selected, such that there are always approximately 5-8 grid points per healing length, depending on the location in the phase diagram. By evaluating the long-range interaction term in momentum space, it is computationally efficient to simulate a single unit cell of the supersolid crystal (for ground-state calculations only) and allow alias Fourier copies of the simulation cell to self-interact [71]. By minimizing the energy per particle with respect to the variational parameters  $\ell$ ,  $\eta$ , and primitive unit cell length  $L_{\text{uc}}$ , it becomes possible to determine the ground state at each point in the phase diagram.

The phase diagram for this system is sketched in Fig. 1 (c), cf. Refs. [15, 16]. In order to characterize the phases of the system, we make use of Leggett's estimate on the upper bound of the superfluid fraction [5],

$$f^s = \frac{L^2}{N} \left[ \int dx \left( \int dy dz |\Psi|^2 \right)^{-1} \right]^{-1}, \quad (6)$$

where  $L = \int dx$ . A value of  $f^s = 1$  indicates the uniform superfluid regime,  $0.1 < f^s < 1$  for the supersolid phase, and  $f^s \leq 0.1$  corresponds to insulating droplets. The boundary to the latter is not captured by our eGPE simulation and the threshold choice of 0.1 is arbitrary, yet the details of this transition are irrelevant to the present work. We will be using  $f^s$  as an order parameter for the superfluid-supersolid transition. The order of the transition depends on the linear density [15, 16],  $\bar{n} = N/L$ , and is discontinuous at both low ( $\bar{n} \lesssim 800 \mu\text{m}^{-1}$ ) and high ( $\bar{n} \gtrsim 4500 \mu\text{m}^{-1}$ ) densities. In the intermediate regime, the transition is continuous and the ground state develops modulation smoothly as the roton mode in the dispersion becomes unstable. In this paper, as a first study of the KZM applied to dipolar supersolids, we restrict our quenches to an intermediate regime in which the transition is expected to be continuous, taking  $\bar{n} = 2500 \mu\text{m}^{-1}$ , for which the superfluid-supersolid transition is found to occur at  $a_s = a_c^{(\text{GS})} \approx 90.5 a_0$ .

## C. Ramp into the supersolid phase

In this work, the initial state is selected to be the ground state of the uniform superfluid regime at  $a_s = 96 a_0$ . Thermal noise at a temperature of  $T = 20$  nK is then added [72] and allowed to equilibrate for 10 ms. We then perform a linear ramp of the scattering length into the supersolid regime to  $a_s = 88 a_0$ , i.e.,  $a_s(t)/a_0 = 96 - 8t/\tau_Q$ , with the ramp time set by  $\tau_Q$ , which takes values between 50 ms and 770 ms throughout this work. The variational parameters are fixed at  $\ell = 1.08 \mu\text{m}$ ,  $\eta = 4.25$ , corresponding to the values in the ground state at  $88 a_0$ . The total system size is selected to be approximately  $L = 344 \mu\text{m}$  such that the ground state achievable by perfect adiabaticity would consist of exactly  $N_{\text{uc}} = 128$  primitive unit cells of the supersolid crystal. See also the Supplemental Material for results at larger system sizes [72]. Statistics are then gathered by performing 500 independent simulations with identical quench parameters.

For the fixed values of the variational parameters above, the critical point of the system is located at  $a_c \approx 91.05 a_0$ . It should be noted that this is slightly shifted from the ground-state critical point  $a_c^{(\text{GS})} \approx 90.5 a_0$  (see previous section, Fig. 1 (b), and Ref. [15]). This shift is expected since  $\ell$  and  $\eta$  vary slightly across the phase diagram and do not remain fixed. We do not expect this effect to have significant impact on our results due to the continuous character of the transition. The shift of the critical point due to fixing the variational parameters is less than the shift set by using the dimensionally reduced theory. In the Supplemental Material, we show some comparisons of our results with full 3D simulations [72].

Fig. 2 shows a sample quench across the superfluid-supersolid transition lasting 100 ms. In Panel (a), a portion of the 1D density as a function of time is shown. Density modulations emerge after the critical point is crossed, with an apparent delay compared to the expectation for an adiabatic crossing of the transition. The nonuniformity of the density modulation front suggests that independent regions begin to form domains at different times. This is further emphasized in panel (b), which shows the full 1D density profile with clearly identifiable regions where the modulation has developed only locally. Panel (c) shows the number of density peaks as a function of time (averaged over 500 independent runs) relative to the expected number in the ground state (128 in this case), showing a smooth development of modulations after the transition is crossed. Furthermore, the quench appears to produce an excess of density modulation peaks, first overshooting the long-time average, and then settling to a value slightly above unity within the time scales we consider here.

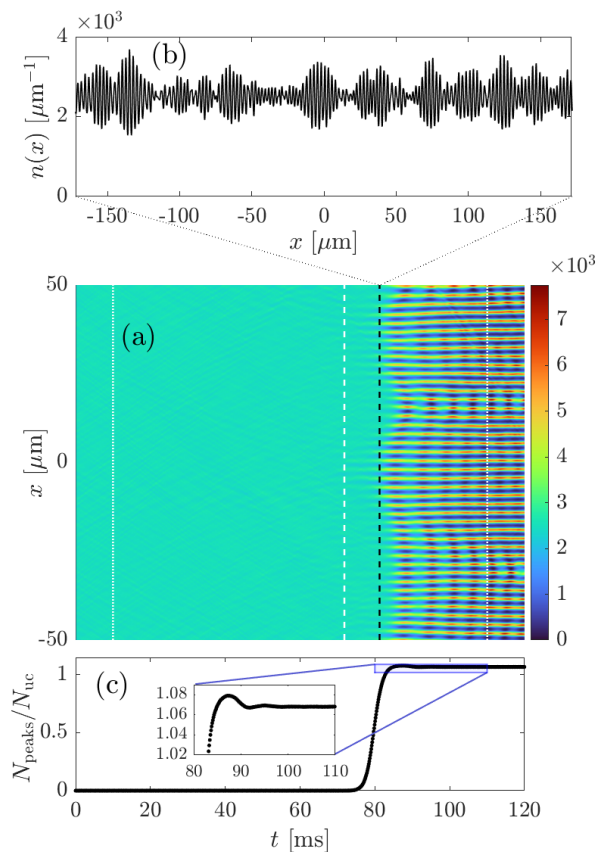


FIG. 2. Quench across the superfluid-supersolid transition. Panel (a) shows the density  $n(z)$  of a part of the system, for a sample quench, equilibrating for 10 ms (leftmost dotted line), then ramping across the critical point (white dashed line) for 100 ms until the final value of  $88 a_0$  (right dotted line) is reached. A density cut along the black dashed line is shown in (b) for the full system. Panel (c) shows the number of supersolid peaks per ground-state unit cell as a function of time for the same quench rate as (a)-(b), averaged over 500 independent noise realizations, with an inset showing an overshoot and rebound following the transition.

### III. SCALING PROPERTIES

#### A. Freeze-out time

According to KZM theory, for a linear quench across a continuous phase transition, the freeze-out time is known to scale as  $\hat{\tau} \propto \tau_Q^{\zeta_{\text{KZ}}}$ , where  $\zeta_{\text{KZ}} = z\nu/(1+z\nu)$  as in Eq. (1). In our system, this indicates that there will exist a quench rate-dependent delay between the crossing of the phase transition and formation of a density modulated superfluid, indicative of a supersolid state.

We characterize the emergence of the density modulation through the evolution of the superfluid fraction, estimated via Eq. (6) and ensemble averaged over 500 realizations. In Fig. 3, we show the dynamics of  $f^s$ , which we take to be an order parameter for the superfluid-supersolid transition. In panel (a), we plot  $f^s$  across

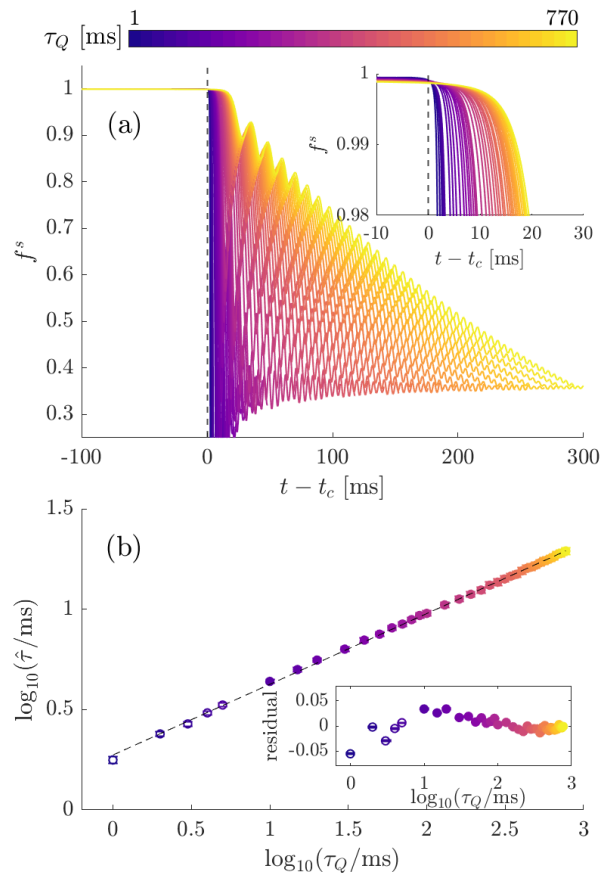


FIG. 3. Delay in supersolid formation for various quenches shown via the decrease of  $f^s$  from unity. Panel (a) shows the full evolution, with the inset focusing on the initial one-dimensional supersolid formation. Slower quenches lead to a greater delay in the formation of a supersolid following the crossing of the critical point. In (b) the time delay  $\hat{\tau}$ , at which the superfluid fraction drops below 0.98, is shown as a function of the quench time  $\tau_Q$ , with the best fit  $\hat{\tau} \propto \tau_Q^{0.352(3)}$  shown as a dashed straight line. Standard errors on the data are shown due to the statistical spread over 500 trials. The inset shows the normalized residuals from the data to the best fit. Open markers represent quenches past  $88 a_0$  (see main text).

the quench, shifted by the time at which the transition is crossed,  $a_s(t_c) = a_c$ , so that all quenches cross the transition at  $t - t_c = 0$ . After a delay, density modulation develops in the system leading to a depression of the superfluid fraction. This reduction is non-monotonic, and there are oscillations in  $f^s$  as the system exhibits a rebounding of the spatial density modulations. This oscillation suggests that an amplitude mode is excited, an example of which is the gapped Higgs excitation that emerges from the roton instability; see Sec. III D and Ref. [71] for a more in-depth discussion of the emergence of this Higgs mode.

In order to avoid the influence of the excited amplitude mode and any coarsening effects it may have on the system, in this section we consider only the onset of super-

solid formation by taking  $\hat{\tau}$  to be defined by the difference between the time at which the critical point is crossed to when  $f^s$  first drops below 0.98, see inset. Using this definition of  $\hat{\tau}$ , in panel (b) we show the scaling as a function of the quench time  $\tau_Q$ . We see clear power-law scaling in agreement with Eq. (1) and fit  $\hat{\tau} \propto \tau_Q^{0.352(3)}$ . For the data in this and subsequent figures, we also plot the normalized residual, for Fig. 3 defined by  $(\hat{\tau} - \text{fit}[\hat{\tau}])/\text{fit}[\hat{\tau}]$ , where  $\text{fit}[\hat{\tau}](\tau_Q) = A \cdot \tau_Q^{\zeta_{\text{KZ}}}$  is the best fit of  $\hat{\tau}(\tau_Q)$  in terms of a pure power law, parametrized by a real constant  $A$  and an exponent  $\zeta_{\text{KZ}}$ .

We select a broad range of quench times to cover what might be considered ‘reasonable’ within an experimental setting, however it should be noted that for inverse rates faster than roughly  $\tau_Q \approx 10$  ms, the quench must be extended past the selected final  $a_s = 88 a_0$ , and eventually into the insulating droplet phase (for all these points we choose a final  $a_s = 60 a_0$ ). This is because for very fast quenches, the finite width of the supersolid region would require stopping the ramp during the freeze-out time, resulting in an effectively nonlinear ramp. Our measures of KZM should not depend on this fact, since we only concern ourselves with initial supersolid formation. However it is important to note that from a practical point of view, there is, generically, an upper limit to how fast one can quench into a supersolid. Throughout the present work, we mark the data obtained by quenches that are taken past the supersolid phase boundary, by open symbols.

## B. Correlation length

During a linear quench, the correlation length remains frozen at a value  $\hat{\xi}$  when entering the freeze-out regime, which, according to KZM theory, scales as  $\hat{\xi} \propto \tau_Q^{\nu_{\text{KZ}}}$ , with  $\nu_{\text{KZ}} = \nu/(1+z\nu)$  cf. Eq. (1). Since the transition to a supersolid is signaled by a growth of periodic diagonal long-range order via density modulations, it can be characterized by the density-density correlation function, viz.,

$$g^{(2)}(x-x') = \frac{1}{\bar{n}^2} \langle \psi^*(x') \psi^*(x) \psi(x) \psi(x') \rangle, \quad (7)$$

where we take  $\langle \dots \rangle$  to indicate an ensemble average, in this case corresponding to a statistical numerical average over 500 independent realizations of the initial noise. Translation invariance allows us to interpret the ensemble average also as a spatial average and so this function is evaluated directly in Fourier space via  $g^{(2)}(x) = \mathcal{F}^{-1}[n(-k)n(k)](x)$ . In Fig. 4(a)-(c), the solid coloured lines show this function for three sample quench rates at the onset of supersolid formation (i.e., when the superfluid fraction is crossing  $f^s(t) = 0.98$ ).

Due to the periodic crystalline structure,  $g^{(2)}$  is highly oscillatory while also decaying towards the background superfluid level. The decay of the initial oscillations indicates that there exists a range over which the supersolid has formed a regular density structure. We find

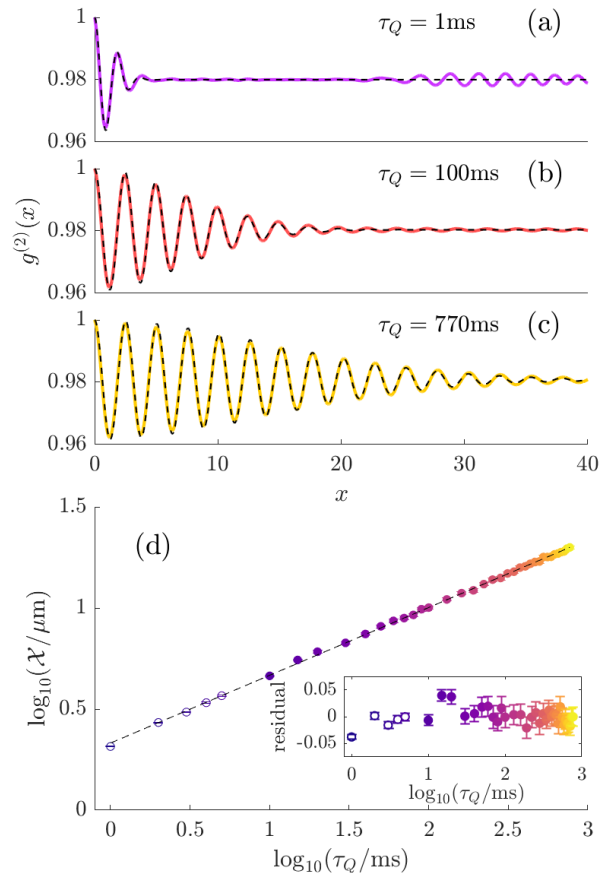


FIG. 4. Scaling of the correlation length. Panels (a)-(c) show the correlation function  $g^{(2)}(x)$  (solid) for  $\tau_Q = \{1, 100, 770\}$  ms, respectively. In each panel,  $g_{\text{fit}}^{(2)}(x)$  is plotted as a black dashed line. Panel (d) shows the width  $\mathcal{X}$  for the fit  $g_{\text{fit}}^{(2)}(x)$  for all quench durations. The best fit  $\mathcal{X} \sim \tau_Q^{0.335(3)}$  is shown as a dashed straight line. Colors and marker filling match Fig. 3. The inset shows the normalized residuals  $(\mathcal{X} - \text{fit}[\mathcal{X}])/\text{fit}[\mathcal{X}]$  of the best power-law fit  $\text{fit}[\mathcal{X}](\tau_Q) = B \cdot \tau_Q^{\nu_{\text{KZ}}}$  of  $\mathcal{X}$ .

that the numerically extracted  $g^{(2)}$  is empirically well-approximated by the function,

$$\text{fit}[g^{(2)}](x) = \mathcal{A} + (1 - \mathcal{A}) \cos(\mathcal{K}x) e^{-x^2/\mathcal{X}^2}, \quad (8)$$

where  $\{\mathcal{A}, \mathcal{K}, \mathcal{X}\}$  are fitting parameters. In general, we expect  $\mathcal{A}$  to match closely with the average background superfluid value  $f^s(t)$ , while the wavevector  $\mathcal{K}$  of the modulation in  $g^{(2)}$  captures the wavevector of the state’s density modulation and should be close to the roton wavenumber  $k_{\text{rot}}$  that triggers the instability. The decay of supersolid correlations is set by the width  $\mathcal{X}$ , which we expect to scale as the correlation length.

In Figs. 4 (a)-(c), the best fit of the function  $g^{(2)}(x)$  is shown as a black dashed line in each panel. Panel (d) shows the fit parameter  $\mathcal{X}$  over all quenches: we are able to observe a clear power-law scaling in agreement with Eq. (1), and plot  $\log_{10}(\mathcal{X}/\mu\text{m})$  together with the corresponding KZM power-law fit,  $\mathcal{X} \sim \hat{\xi} \sim \tau_Q^{0.335(3)}$ . Similar

scaling can be extracted by simply considering the width of a root-mean squared envelope of  $g^{(2)}(x)$  as the oscillations decay (not shown here). The decaying envelope indicates that regular periodic order is not maintained globally across the crystal, but rather that the system forms locally regular domains that are globally incommensurate. There also appears to be a small revival in supersolid coherence in panel (a) that is not captured by our fitting function. We expect that revivals of this kind become less relevant with larger statistical ensembles.

### C. Crystal phase and defect densities

Another way to define supersolid correlation is to identify a spatially-varying crystal phase along the full system and evaluate the phase coherence over space. This definition is instructive and allows us to directly identify the defects in the crystal structure through phase jumps. Below we describe how to define the crystal phase, check the scaling of the correlation length through that of the crystal phase coherence, and study the scaling of the number of defects.

The local phase  $\phi$  of the crystal at a point  $x = x_j$  can be defined in the following way,

$$\phi(x_j) = \frac{2\pi}{\bar{d}} (x_j - j\bar{d}), \quad (9)$$

where  $\bar{d} = N_{\text{peaks}}^{-1} \sum_j' (x_{j+1} - x_j)$  is the average peak-to-peak distance, and the prime indicates that the sum is taken over the density peaks, numbered from  $j = 1$  to  $N_{\text{peaks}}$ . This phase is schematically depicted in Fig. 5 (a), defining  $\phi(x_j)$  as the normalized distance of the individual peaks from their respective adjacent minimum in some reference lattice with lattice constant  $\bar{d}$  (vertical dashed lines). In analogy with a perfectly coherent uniform superfluid, a globally coherent crystal would therefore have  $\phi(x_j) = \text{constant}$ . Numerically, this phase is the phase factor of a Fourier transform of each unit cell of size  $\bar{d}$ .

The supersolid coherence can also be quantified via its corresponding crystal phasor  $e^{i\phi(x)}$  and its two-point correlation function,

$$C(x - x') = \langle e^{-i\phi(x)} e^{i\phi(x')} \rangle. \quad (10)$$

Unlike for  $g^{(2)}$ , the phase  $\phi(x)$  is, in each run, only evaluated at the (randomly located) positions  $x_j$  of the density maxima, which results in a much coarser structure. Fig. 5 (b) shows the crystal correlation function (10) following the quench, at the moment  $t$  when the superfluid fraction drops below  $f^s(t) = 0.98$ , i.e. at  $t = \hat{\tau}$ . The width at half maximum of  $C(x)$  is proportional to the correlation length  $\hat{\xi}$  at the freeze-out time and is then plotted as a function of quench time in panel (c). The extracted correlation length shows power-law scaling,  $\hat{\xi} \propto \tau_Q^{0.275(3)}$ , a somewhat smaller estimate than the scaling of  $g^{(2)}$ . In

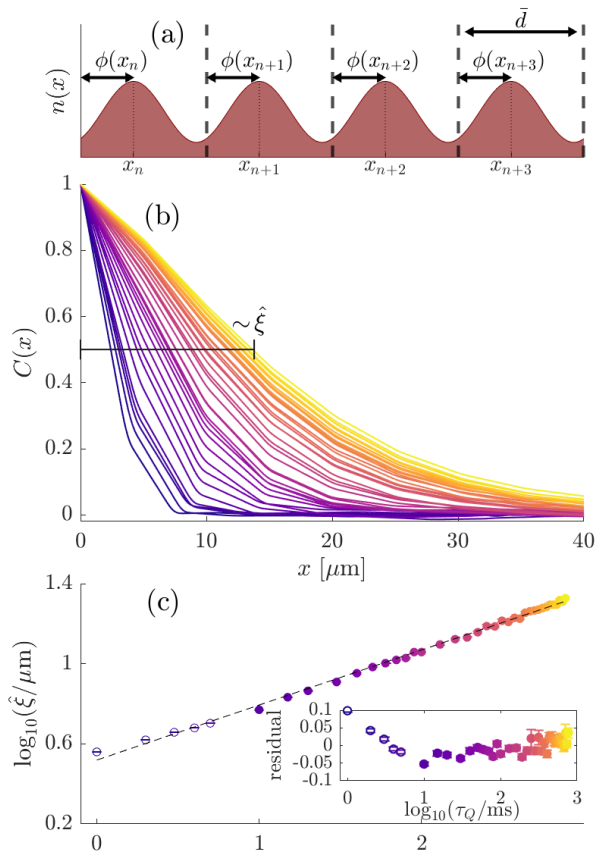


FIG. 5. Crystal phase and correlation function  $C(x)$ . A schematic for the crystal phase is shown in (a), where a modulated supersolid density structure with (in general unevenly spaced) peaks at  $x_j$ , marked with dotted lines. The normalized distance from those peaks to some reference set of points equally spaced by  $\bar{d}$ , shown as vertical dashed lines, gives the crystal phase  $\phi(x_j)$  at that peak. Panel (b) shows the correlation function (10) for the same quenches as used for Fig. 3. The half width at half maximum is depicted in panel (c), together with the power-law fit  $\hat{\xi} \propto \tau_Q^{0.275(3)}$ , with the normalized residuals computed in analogy to those in Fig. 3 and shown in the inset. Colors and marker filling for (b)-(c) match those in Fig. 3.

Appendix VD, we discuss the close relationship between  $C(x)$  and  $g^{(2)}(x)$ .

In computing  $C(x)$ , it is the averaging over hundreds of trials that ultimately smooths out the data. From the resulting averages one obtains a smooth function that nevertheless develops kinks where its slope changes suddenly due to the higher likelihood of finding a lattice site below that distance. Importantly, at faster quenches, the separation of scales begins to break down: the width of  $C(x)$  becomes on the order of the density modulation periodicity  $L_{\text{uc}} \approx 2.6 \mu\text{m}$ . Without the separation of scales, the notion of a KZM domain and a supersolid defect become poorly defined [73].

KZM-induced supersolid defects in the one-dimensional system can be understood as sudden

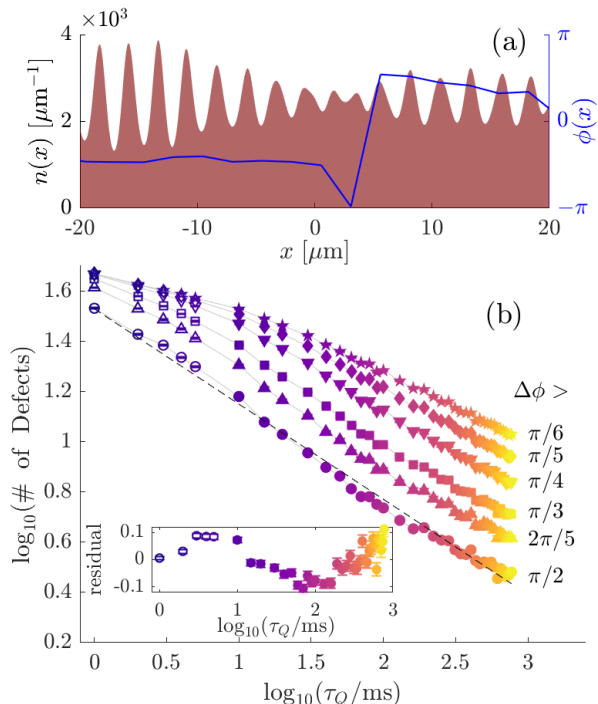


FIG. 6. Defect density scaling. Panel (a) illustrates a crystal defect from one simulation run in the density  $n(x)$  (brown shaded area) and the crystal phase  $\phi(x)$ . Defects are identified as local jumps in the crystal phase  $\phi(x)$ . Panel (b) reports on the number of crystal defects observed at the supersolid formation time for different minimum thresholds of phase jumps,  $\Delta\phi > \{\pi/6, \pi/5, \pi/4, \pi/3, 2\pi/5, \pi/2\}$ , marked as {circles, triangles, squares, inverted triangles, diamonds, stars}, respectively. Light gray lines along data sets with the same defect size are shown to guide the eye. The best fit line for  $n_d \propto \tau_Q^{-\nu_{\text{KZ}}}$  is shown for  $\Delta\phi > \pi/2$  only (dashed). Normalized residuals determined in analogy to those in Fig. 3 are shown in the inset. Colors and marker filling for (b) match those in Fig. 3.

jumps in the crystal phase  $\phi$ , noted  $\Delta\phi$ . Based on the fundamental predictions of KZM theory quoted above, the defect density can be estimated to scale as,

$$n_d \sim \frac{\xi^d}{\xi^D} \sim \left(\frac{1}{\tau_Q}\right)^{(D-d)\frac{\nu}{1+\nu}} \equiv \tau_Q^{(d-D)\nu_{\text{KZ}}}, \quad (11)$$

where  $d$  and  $D$  are the dimensionality of the defects and system, respectively. In the case of sudden kinks in the crystal phase alone, we therefore expect our results to correspond to  $d = 0$  and  $D = 1$ , indicating that the defect density scaling should match that of  $\hat{\xi}$ .

In Fig. 6, we plot the number of defects ( $\propto n_d$ ) as a function of quench rate. Due to the continuous nature of  $\phi$ , there remains some ambiguity as to the required size of crystal phase jump to correspond to a defect. We therefore show the scaling for a range of phase jumps corresponding to  $\Delta\phi > \{\pi/6, \pi/5, \pi/4, \pi/3, 2\pi/5, \pi/2\}$ . In all cases, a clear scaling of the number of defects with the quench rate is observed. At faster quench rates, the data

appear to curve and saturate towards a behavior that indicates that the defect density begins to be independent of the quench rate. In our case, we again attribute this to the breakdown of scale separation in our system: typical KZM domain sizes begin to approach the crystal wavelength, below which any notion of a supersolid defect becomes poorly defined. This saturation behavior has also been seen in other systems [49, 52, 55] and has been described in terms of a universal breakdown [74] of the KZM at fast quench rates.

In order to select an appropriate definition of a crystal defect, we consider their number distribution statistics. Assuming that the number of defects formed due to the KZM corresponds to a random quantity extracted from fundamentally independent trials, we therefore expect the probability of counting  $\mathcal{N}$  defects to obey a Poisson distribution,

$$P(\mathcal{N}) = \frac{1}{\mathcal{N}!} \lambda^{\mathcal{N}} e^{-\lambda}. \quad (12)$$

The expected value  $\lambda = \langle \mathcal{N} \rangle$  is then set by the quench rate according to the KZM scaling.

For a selection of defect sizes and quench rates, we plot, in Fig. 7, the defect count probabilities within our total system following a quench, and compare them to the best-fit Poisson distribution curves  $P(\mathcal{N})$ . The difference of the curves is quantified through the average sum of squared residuals (RSS). A stricter definition of a defect (i.e., larger  $\Delta\phi$ ) leads to better agreement (smaller RSS) with Poisson distributions across different  $\tau_Q$ , while smaller phase jumps yield narrow peaks that disagree with the Poissonian hypothesis, especially at fast quench rates. Deviations from Poisson statistics imply that the phase jumps being counted no longer result from independent random events and thus are no longer ‘defects’ in the KZM sense, but are somehow correlated. We suspect that small changes in the crystal regularity may not only arise due to KZM scaling, but as excitations in the crystal due to propagation of, e.g., sound modes (phonons) within an otherwise coherent domain.

The analysis of Fig. 7 indicates that a strict definition of a defect, using a large minimal phase jump  $\Delta\phi > \pi/2$  is required for identifying KZM defects. Returning to Fig. 6 we fit the  $\tau_Q$ -scaling of the numbers of defects with  $\Delta\phi > \pi/2$  with a power law and extract  $\nu_{\text{KZ}} = \frac{\nu}{1+\nu} \approx 0.37(2)$ . This scaling measure is independent from the  $g^{(2)}$  scaling of the correlation length in Sec. III B, and again appears to give a scaling result relatively close to  $1/3$ , albeit it is slightly outside the standard error bounds. We would like to also remark here that considering defects with large phase jumps may introduce a larger statistical spread: With the system sizes we simulate here, slow quench rates may only produce a handful of defects ( $\lesssim 5$ ), and so the relative point spread error due to a single defect can be large. In the following section, we shall further examine the compatibility of these results with respect to critical scaling exponents as extracted from Bogoliubov theory.

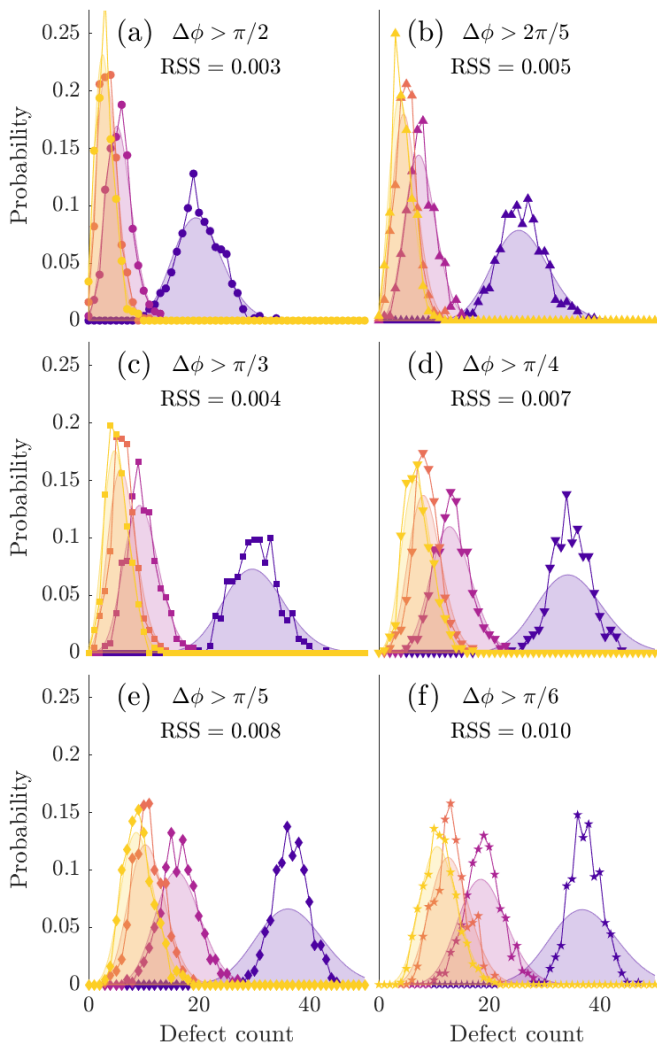


FIG. 7. Defect counting statistics. The probability of occurrence of a certain number of phase jumps within a fixed system size  $L$  is plotted (filled symbols) for different  $\tau_Q \in \{10, 100, 404, 709\}$  ms, and different  $\Delta\phi$  (see panel captions). Symbols match those in Fig. 6). The Poisson distribution corresponding to the maximum likelihood estimate for  $\lambda$  for each dataset is shown as a shaded area. Lines serve as a guide to the eye. The residual sum of squares (RSS) is quoted in each panel. Colors match those in Fig. 3

We note that, in the above analysis, we did not consider the influence of extended ( $d = 1$ ) excitations playing a role in supersolid formation. It is known that, for the temperature-quench-induced BEC transition [49, 56], the interplay between defects of different dimensions (e.g. vortices vs. solitons) may hybridize the scaling result of Eq. (11). Similarly, any incidence of nonlinear excitations induced by the transition or by the initial thermal fluctuations would therefore, in principle, also contribute to the flattening of the curves in Fig. 6.

#### D. Scaling exponents

Using the numerical results for  $\zeta_{\text{KZ}}$  and  $\nu_{\text{KZ}}$  from subsections III A and III B, respectively, we extract the scaling exponents,

$$\nu = 0.57(1), \quad (13)$$

$$z = 1.05(2), \quad (14)$$

for the superfluid-to-supersolid transition.

We may compare these dynamical KZM results to equilibrium estimates. The characteristic time scale of a system near a quantum critical point is determined by the inverse of the energy gap, which closes as  $\Delta \sim |\lambda - \lambda_c|^{z\nu}$  near the critical value  $\lambda_c$  of some tuning parameter  $\lambda$  [75]. Meanwhile, in the theory of dynamical critical phenomena [76] the low-energy vs. low-momentum scaling of the dispersion defines the dynamical critical exponent as  $\omega \propto k^z$ . In the uniform superfluid, the dispersion relation can be calculated analytically within Bogoliubov theory [69],

$$\hbar\omega = \sqrt{\frac{\hbar^2 k^2}{2m} \left( \frac{\hbar^2 k^2}{2m} + \frac{6\gamma_{\text{QF}} n^{3/2}}{5\pi^{3/2} \ell^3} + \frac{gn}{\pi \ell^2} + 2n\tilde{U}^{1\text{D}}(k) \right)}, \quad (15)$$

while in the supersolid phase only numerical solutions are possible. At zero temperature and for  $a_s > a_c \approx 91.05 a_0$ , there exists a single gapless low-energy sound branch (i.e. Goldstone mode) associated with the phase rigidity of the system. At higher  $k$ , the attractive contribution of the DDI results in a rotonic minimum at momentum  $k = k_{\text{rot}}$  and of energy  $\epsilon_{\text{rot}}$ , and it is the softening and instability of the roton mode that leads to supersolid formation, see e.g. [15]. Fig. 8 (a) shows the dispersion relation in the uniform regime (green curves), with a roton minimum developing as  $a_s$  is reduced. In the regime of the phase diagram where the transition is continuous, the onset of supersolidity occurs as the roton minimum touches zero,  $\epsilon_{\text{rot}} = 0$  (black curve,  $a_s = a_c$ ), and proceeds to go unstable.

The emergence of periodic density modulation in real space also leads to a periodic dispersion in momentum space and thus to a band structure. Fig. 8 (b) shows the band structure precisely at the critical point, with the Brillouin zone (BZ) edges set at multiples of the roton momentum at criticality,  $k_{\text{rot}} \equiv k_c$ , see e.g. [71]. This corresponds to the mapping of the dispersion relation at  $a_s = a_c$  of panel (a) into the first BZ. In this mapping, the roton minimum yields a second Goldstone (crystal-sound) mode associated with the breaking of the translational symmetry, and a third branch, which appears gapless at the transition. Precisely at the critical point, the roton wavelength sets the unit cell length via  $L_{\text{uc}} = 2\pi/k_c$ ; however, the unit cell size does not remain constant throughout the supersolid regime. Just below the transition, as shown in panel (c) for  $a_s = 90 a_0$ , the dispersion relation show two gapless Goldstone mode while a gap (re)opens in the first branch at  $k = \{0, k_c, 2k_c, \dots\}$ ,



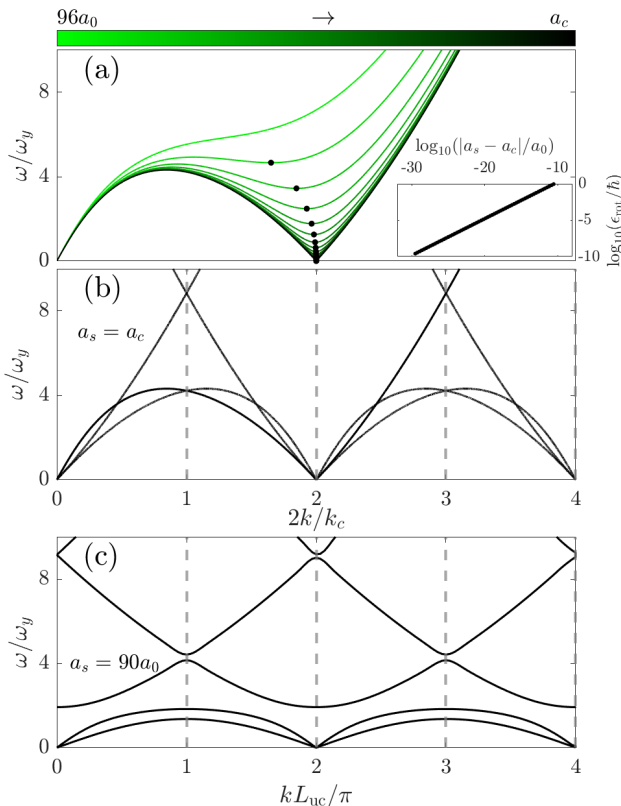


FIG. 8. Panel (a) show the dispersion relation and the closing of the roton gap from Bogoliubov theory (Eq. (15)) as  $a_s$  is tuned through the superfluid regime. The roton minimum is marked by black circles. The scaling of the roton gap as  $a_s$  approaches  $a_c \approx 91.05 a_0$  from above is shown in the inset and satisfies  $\epsilon_{\text{rot}} \sim \sqrt{a_s - a_c}$ . Panel (b) shows the mapping of the spectrum at the critical point [black curve in (a)] into a periodic Brillouin-zone structure with periodicity  $k_{\text{rot}} \equiv k_c$ . Panel (c) shows the dispersion in the supersolid regime with a periodic Brillouin-zone structure whose periodicity is  $2\pi/L_{\text{uc}}$ . BZ edges are marked as vertical grey dashed lines. The excitation frequencies  $\omega$  are shown in units of the transverse trapping frequency  $\omega_y = \omega_z = 2\pi \times 150$  Hz.

corresponding to the Higgs mode that drives the amplitude of density modulations.

Within Bogoliubov theory, we therefore expect the characteristic time to scale inversely to the closing of the rotonic energy gap [75],

$$\tau^{-1} \sim \epsilon_{\text{rot}} \sim |a_s - a_c|^{z\nu}. \quad (16)$$

It has been previously shown [69], and is verified here in the inset to Fig. 8 (a), that the roton gap closes as  $\epsilon_{\text{rot}} \sim \sqrt{a_s - a_c}$  so that  $z\nu = 1/2$ . Meanwhile, precisely at the critical point, the dispersion relation linearizes around the roton momentum,

$$\epsilon_{\text{rot}} \propto |k - k_c|, \quad (17)$$

and from the BZ mapping, the gapless roton mode emerges periodically about the zone edges,  $\epsilon_{\text{rot}} \propto |k -$

$mk_c|$ ,  $m \in \mathbb{Z}$ . Due to the linearization of the dispersion relation around  $mk_c$ , for the superfluid to one-dimensional supersolid transition considered here, Bogoliubov theory suggests  $z = 1$ .

The scaling exponents extracted from our numerical simulations,  $\nu = 0.57(1)$  and  $z = 1.05(2)$ , appear compatible with the mean-field scaling exponent,  $\nu = 1/2$ , of the correlation length and the quantum-critical value  $z = 1$  of the dynamical exponent, although these fall slightly outside the statistical error bars of our results. We note that the critical scaling behavior may be modified compared to that anticipated from mean-field theory due to beyond-mean-field fluctuations. A universality class that we had foreseen to apply to our transition is that of the  $(D+1)$ -dimensional XY model, with  $D_{\text{lc}} = 1$  and  $D_{\text{uc}} = 3$  being the respective lower and upper critical dimensions. In our case,  $D = 1$ , such that the transition would be of the Berezinskii-Kosterlitz-Thouless (BKT) type [77–80], for which a non-polynomial correlation length and relaxation time scaling could be expected, which reaches power-law scaling with  $\nu \rightarrow \infty$ ,  $z = 1$  only asymptotically, for exponentially large quench times  $\tau_Q$  [78]. This is in contrast to the clean power-law scaling observed here already for relatively small  $\tau_Q$ , resulting in the above near-mean-field value of the exponent  $\nu$ . Furthermore, Blakie *et al.* [71], who examined the critical behavior at the continuous superfluid-supersolid transition line, using Bogoliubov theory, found that there is a discontinuity in the compressibility, consistent with the transition being second-order (the single exception being at the tip of the phase transition curve, which we do not encounter in any quenches performed in this paper). This discontinuity contrasts with the BKT expectation and supports the hypothesis of a universality class different from  $(1+1)$ D XY. Even in  $D = 3$  spatial dimensions, i.e., at the upper critical dimension of the XY model, the exponents, near the quantum critical point, would receive small anomalous contributions, and  $z \simeq (D+1)/2 = 2$  instead of the exponent  $z \simeq 1$  we find, which is indeed compatible with dynamical critical scaling in  $D = 1$  dimensions [76]. The exact universality class of the transition remains undetermined. We, however, note that our extracted near-mean-field exponents have been previously found to characterize the universality class for the superfluid-to-Mott insulator transition in the Bose-Hubbard model in  $D \geq 3$  spatial dimensions, when crossing precisely at the Mott lobe tips with integer filling factor, i.e., at the quantum multicritical point [81, 82], and exponents similar to our KZM results have been previously observed in density-wave order (supersolid) transitions in  $D = 2$  dimensions [83].

#### IV. CONCLUSION

We have explored the formation of a supersolid in an elongated dipolar quantum gas following a quench of the scattering length, using a reduced 3D model and

via the extended Gross-Pitaevskii equation. We extract power-law scaling exponents corresponding to diverging relaxation time and correlation length scales. In particular, the divergence in relaxation time was estimated by identifying the freeze-out time with the delay in supersolid formation during the quench. The supersolid correlation length scaling was extracted by fitting a spatially oscillating function with Gaussian-shape envelope to the density-density correlation function  $g^{(2)}(x)$ . We found that the results for the extracted critical exponents,  $\nu = 0.57(1)$  and  $z = 1.05(2)$ , appear to be nearly compatible with the corresponding values expected from mean-field theory. When considering a measure for the crystal phase,  $\phi(x)$ , we found that there appears to be a systematic breakdown of scaling results and an onset of defect density saturation at very fast quench rates. We posit that this breakdown [74] is explained by the fact that typical KZM domain sizes in the supersolid approach the crystal lattice size set by the roton. Nevertheless, over multiple orders of magnitude, defect densities appear to obey power-law scaling.

We consider an elongated system for statistical purposes, however our study is performed with experimental considerations in mind. In particular, we selected parameters corresponding to  $^{164}\text{Dy}$ , including scattering lengths, typical trap frequencies, and reasonable temperatures used in dipolar quantum gas experiments [9–11]. For a dipolar gas confined in a harmonic trap, the direct applicability of our results will depend on the cloud aspect ratio and quench rates [40], since in some regimes the inhomogeneous KZM [32, 56] may lead to a different set of exponents. One candidate for the uniform tubular geometry we have proposed is a ring-shaped trap [84], which has been realized for  $^{23}\text{Na}$  [85–88] and  $^{87}\text{Rb}$  [46, 89–94], and has been theoretically shown to support the dipolar supersolid phase [95, 96]. While supersolid lifetimes remain a challenge for these experiments, particularly due to high densities in the dipolar droplets, the advantage of the measures we have introduced in this paper is that only the onset of supersolidity needs to be considered, thus long lifetimes are not required to verify our results. In this work, we have only focused on the transition from the uniform superfluid to one-dimensional droplet chain. If an additional trapping direction is relaxed, there exist transitions to many more kinds of two-dimensional supersolid lattices that are also possible, leaving the door open to further examination of dynamical symmetry breaking in more complex supersolids.

## ACKNOWLEDGMENTS

The authors thank M. Ballu, R. Bisset, T. Bland, K. Chandrashekhara, J. Gao, C. Götzhäuser, P. Heinen, L. Hoenen, G. Lamporesi, A. Oros, E. Poli, G.-X. Su, and N. Rasch for helpful discussions and collaboration on related work. They acknowledge support by the Deutsche

Forschungsgemeinschaft (DFG, German Research Foundation), through SFB 1225 ISOQUANT (Project-ID 273811115), grant GA677/10-1, and under Germany's Excellence Strategy – EXC 2181/1 – 390900948 (the Heidelberg STRUCTURES Excellence Cluster), and by the state of Baden-Württemberg through bwHPC and the DFG through grants INST 35/1134-1 FUGG, INST 35/1503-1 FUGG, INST 35/1597-1 FUGG, and 40/575-1 FUGG (MLS-WISO, Helix, and JUSTUS2 clusters). W.K. acknowledges the support of the Natural Sciences and Engineering Research Council of Canada (NSERC), [funding reference number PDF-577924-2023]. L.C. acknowledges support by the European Research Council (ERC) under the European Union's Horizon Europe research and innovation program under grant number 101040688 (project 2DDip). Views and opinions expressed are however those of the authors only and do not necessarily reflect those of the European Union or the European Research Council. Neither the European Union nor the granting authority can be held responsible for them.

## V. SUPPLEMENTARY

### A. Thermal and quantum noise

In the variational 1D simulations, thermal and quantum noise is included via,

$$\psi(x, 0) = \sqrt{\bar{n}} + \sum'_s [A_l^+ e^{ik_l x} + A_l^- e^{-ik_l x}], \quad (18)$$

where  $A_l^\pm$  are Gaussian random variables subject to  $\langle |A_l^\pm|^2 \rangle = \langle |A_l^\mp|^2 \rangle = e^{(\epsilon_l^f - \mu)/k_B T}$  for temperature  $T$  and free-particle dispersion  $\epsilon_l^f = 2\hbar^2 l^2 / (mL^2)$  for  $l \in \mathbb{N}^+$ . The sum  $\sum'$  is restricted to eigenstates such that  $\epsilon_l^f < 2k_B T$ .

In full 3D calculations (see Sec. VB), thermal and quantum noise includes amplitudes in the transverse harmonic oscillator modes,

$$\Psi(\mathbf{r}, 0) = \sqrt{\bar{n}} + \sum'_{l\gamma\delta} \phi_\gamma(y) \phi_\delta(z) [A_{l\gamma\delta}^+ e^{ik_l x} + A_{l\gamma\delta}^- e^{-ik_l x}], \quad (19)$$

where now  $\langle |A_{l\gamma\delta}^+|^2 \rangle = \langle |A_{l\gamma\delta}^-|^2 \rangle = e^{(\epsilon_{l\gamma\delta} - \mu)/k_B T}$  for dispersion  $\epsilon_{l\gamma\delta} = \hbar\omega_y (\gamma - \frac{1}{2}) + \hbar\omega_z (\delta - \frac{1}{2}) + 2\hbar^2 l^2 / (mL^2)$ , now with  $l, \gamma, \delta \in \mathbb{N}^+$ . The sum has again been restricted such that  $\epsilon_{l\gamma\delta} < 2k_B T$ .

### B. Comparison with 3D simulations

Here, we compare our results with full 3D simulations, i.e. evolving under Eq. (2), for select quench rates. Similar to the variational model, we perform quenches from  $a_s = 96 a_0$  to  $a_s = 88 a_0$ , now with a grid size of approximately  $\approx 160 \mu\text{m}$ , corresponding to 64 unit cells in the

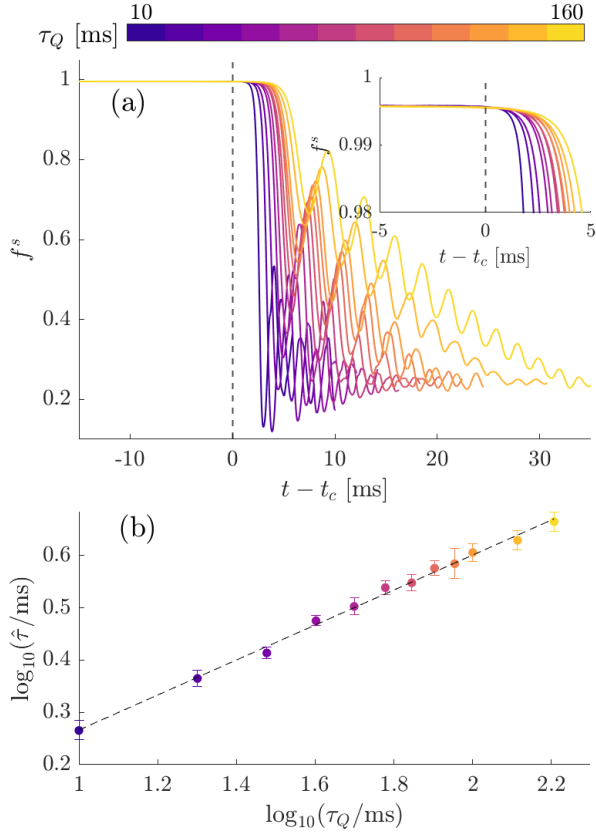


FIG. 9. Delay in supersolid formation for various quenches for full 3D simulations. Similar to Fig. 3 of the main text, panel (a) shows the full  $f^s(t)$ , with the inset focusing on the initial supersolid formation. Panel (b) shows the time delay at which  $f^s$  crosses 0.98, indicating supersolid formation, with the best fit  $\hat{\tau}_{3D} \propto \tau_Q^{0.33(1)}$  shown as a dashed line. Note, the difference in colorbar scale from the other figures due to the limited range of  $\tau_Q$ .

supersolid ground state at  $88a_0$ . At  $\bar{n} = 2500 \mu\text{m}^{-1}$ , 3D simulations indicate that the critical point is located at  $a_s = a_c^{3D} = 92.27a_0$  [16]. Due to the size of the simulation grids and the resulting datasets, the results are averaged over only 5 realizations each of the noise in Sec. V A, and for a more limited range of  $\tau_Q$ , resulting in much larger standard errors in the data.

The superfluid fraction  $f^s$  as a function of time is presented in Fig. 9 (a). Similar to the main text, we can extract the supersolid delay by the time it takes for  $f^s$  to drop below 0.98. The scaling of the delay is plotted in panel (b), along with the corresponding quench data using the variational model. We are able to extract  $\hat{\tau}_{3D} \propto \tau_Q^{0.33(1)}$ , which, within the error range quoted, is compatible with our results from the reduced model.

We can also measure the  $g^{(2)}$  correlation function along the  $z$ -axis for full 3D simulations, as shown in Fig. 10. Similar to Fig. 4 of the main text, we plot in panels (a)-(c) the correlation function  $g^{(2)}(x)$ , now after integrating out the wavefunction in the radial directions,

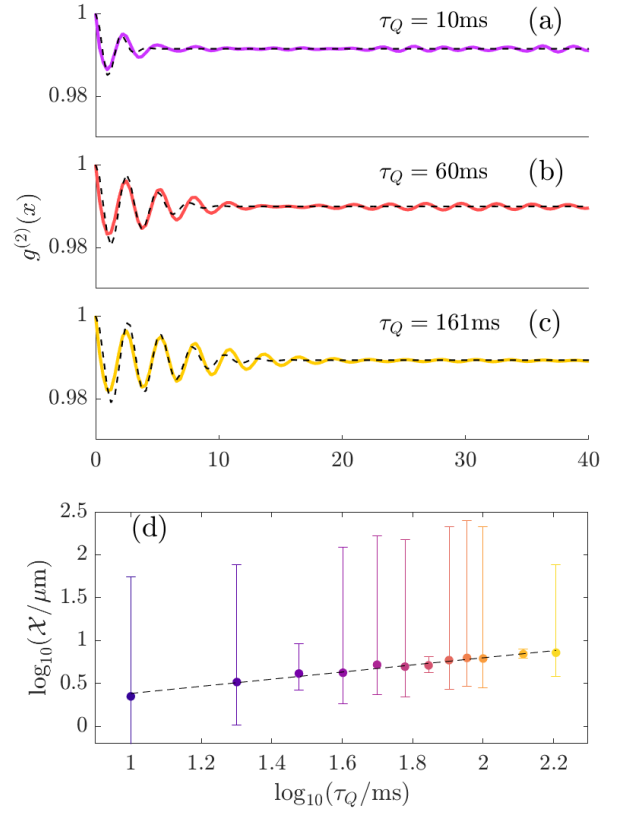


FIG. 10. Supersolid correlation length  $g^{(2)}(x)$ , similar to Fig. 4, now for 3D simulations, at  $\tau_Q = \{10, 60, 161\}$  in panels (a)-(c), respectively. A giving an approximate scaling of  $\mathcal{X} \sim \hat{\xi} \sim \tau_Q^{0.40(16)}$ .

$\psi(x) = \int dy dz \Psi(\mathbf{r})$ , for  $\tau_Q = \{10, 60, 161\}$ , respectively. Panel (d) shows the best fit  $\mathcal{X}$  from Eq. (8), giving an approximate scaling of  $\mathcal{X} \sim \hat{\xi} \sim \tau_Q^{0.40(16)}$ .

### C. System length dependence

In this section, we present results for the freeze-out time and correlation functions in our reduced theory for system sizes consisting of 1024 unit cells, compared to 128 of the main text. The aim of this section is to verify that finite-size effects do not strongly affect the main results of the paper. Due to the large size of the system, we only perform 10 quenches for each  $\tau_Q$ .

Fig. 11 shows the superfluid fraction over time in the longer system, governed by Eq. (5). The results for the freeze-out time appear to be similar to the results of the shorter system in the main text, with an extracted scaling of  $\hat{\tau}_{\text{long}} \propto \tau_Q^{0.344(1)}$ . This result is not unexpected: for a uniform system, the delay in supersolid formation should not depend on the system size. It is notable that relatively few trials are sufficient to give similar results to the main text.

In Fig. 12 we show the correlation function  $g^{(2)}(x)$  sim-

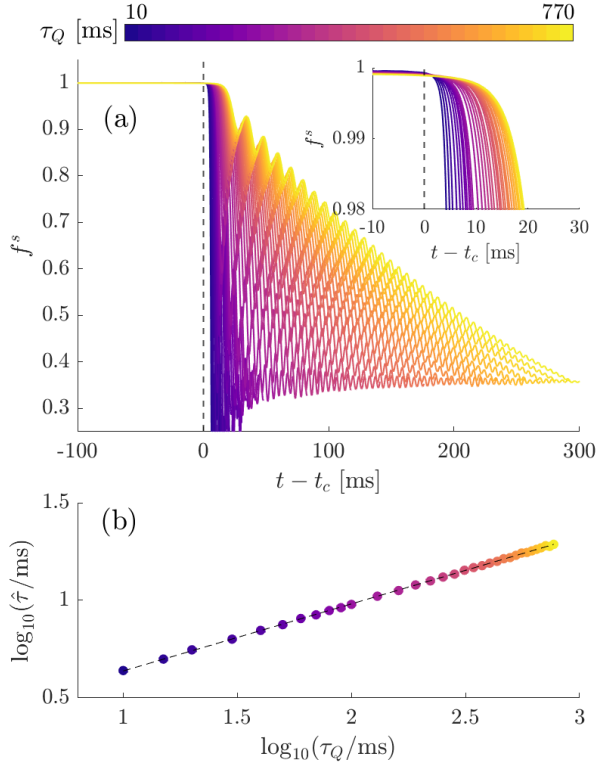


FIG. 11. Delay in supersolid formation in the reduced theory for a much longer system size of 1024 unit cells. Similar to Fig. 3 of the main text, panel (a) shows the full  $f^s(t)$ , along with a zoomed-in inset. Panel (b) gives the log-log time delay at which  $f^s$  crosses 0.98, with the best fit as a dashed line.

ilarly to Fig. 4 of the main text, now for the longer system. We again perform a fit according to Eq. (8) at the onset of supersolid formation, and extract a scaling result of  $\mathcal{X} \sim \hat{\xi} \sim \tau_Q^{0.332(8)}$ , similar to the main text. Due to the fact that  $g^{(2)}(x)$  is spatially averaged over a much longer system, the results presented here do not suffer from any dramatic loss of statistics due to averaging over only 10 quenches. However, the limited number of quenches does prevent us from achieving statistically meaningful results in terms of defect counting, so we do not attempt any analysis of defect density scaling in the longer system.

#### D. Relationship between $g^{(2)}$ and $C(x)$

Assuming the following ansatz for the density,

$$n(x) = \bar{n} + \lambda \cos(kx + \phi(x)), \quad (20)$$

where  $\phi(x)$  is some locally varying phase, and  $\lambda$  is the strength of the supersolid modulation, the correlation

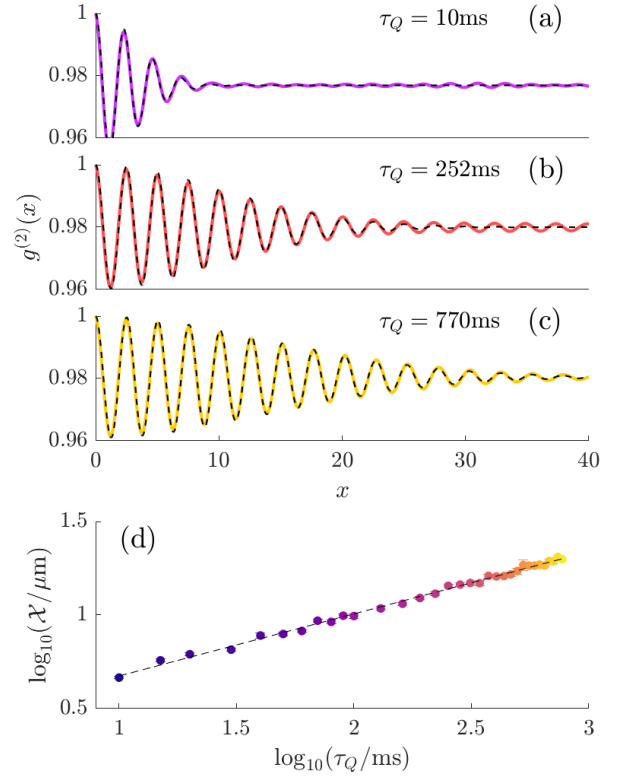


FIG. 12. Supersolid correlation length  $g^{(2)}(x)$ , similar to Fig. 4, now for long system sizes of 1024 unit cells, at  $\tau_Q = \{10, 252, 770\}$  in panels (a)-(c), respectively. The best fit of  $\mathcal{X}$  using Eq. (8) is shown as a dashed line.

function can be determined from

$$\begin{aligned} n(x)n(x') &= [\bar{n} + \lambda \cos(kx + \phi(x))] \\ &\quad \times [\bar{n} + \lambda \cos(kx' + \phi(x'))] \\ &= \bar{n}^2 + \bar{n}\lambda [\cos(kx + \phi(x)) + \cos(kx' + \phi(x'))] \\ &\quad + \lambda^2 \cos(kx + \phi(x)) \cos(kx' + \phi(x')) \\ &= \bar{n}^2 + \bar{n}\lambda [\cos(kx + \phi(x)) + \cos(kx' + \phi(x'))] \\ &\quad + \frac{\lambda^2}{4} [e^{i(kx + \phi(x))} + e^{-i(kx + \phi(x))}] \\ &\quad \times [e^{i(kx' + \phi(x'))} + e^{-i(kx' + \phi(x'))}]. \quad (21) \end{aligned}$$

Averaged over realizations, terms like  $\cos(kx + \phi(x))$  will vanish, leaving

$$\begin{aligned} \langle n(x)n(x') \rangle &= \bar{n}^2 + \frac{\lambda^2}{4} \langle e^{i(k(x+x') + \phi(x) + \phi(x'))} \\ &\quad + e^{i(k(x-x') + \phi(x) - \phi(x'))} + \text{h.c.} \rangle \\ &= \bar{n}^2 + \frac{\lambda^2}{4} \langle e^{2ikR} e^{i(\phi(x) + \phi(x'))} \\ &\quad + e^{i(ks + \phi(x) - \phi(x'))} + \text{h.c.} \rangle, \quad (22) \end{aligned}$$

where we let  $s = x - x'$  and  $R = (x + x')/2$ . Let us now concern ourselves only with the terms that depend

directly on the difference between two points, i.e.,

$$\langle e^{iks} e^{i\phi(x)} e^{-i\phi(x')} + e^{-iks} e^{-i\phi(x)} e^{i\phi(x')} \rangle. \quad (23)$$

In principle, if one removes the oscillatory behavior of  $\langle n(x)n(x') \rangle$ ,  $e^{iks}$ , then we can write  $g^{(2)}(x)$  as a sum of

functions like  $C(x)$ , and therefore  $C(x)$  should describe the decay of  $g^{(2)}(x)$ .

- 
- [1] O. Penrose and L. Onsager, Bose-Einstein condensation and liquid helium, *Phys. Rev.* **104**, 576 (1956).
- [2] E. P. Gross, Unified theory of interacting bosons, *Phys. Rev.* **106**, 161 (1957).
- [3] E. Gross, Classical theory of boson wave fields, *Annals of Physics* **4**, 57 (1958).
- [4] A. Andreev and I. Lifshitz, Quantum theory of defects in crystals, *J. Exp. Theo. Phys.* **56**, 2057 (1969).
- [5] A. J. Leggett, Can a solid be "superfluid"?, *Phys. Rev. Lett.* **25**, 1543 (1970).
- [6] M. Boninsegni and N. V. Prokof'ev, Colloquium: Supersolids: What and where are they?, *Rev. Mod. Phys.* **84**, 759 (2012).
- [7] J.-R. Li, J. Lee, W. Huang, S. Burchesky, B. Shteynas, F. Ç. Top, A. O. Jamison, and W. Ketterle, A stripe phase with supersolid properties in spin-orbit-coupled Bose-Einstein condensates, *Nature* **543**, 91 (2017).
- [8] A. Putra, F. Salces-Cárcoha, Y. Yue, S. Sugawa, and I. B. Spielman, Spatial coherence of spin-orbit-coupled Bose gases, *Phys. Rev. Lett.* **124**, 053605 (2020).
- [9] L. Tanzi, E. Lucioni, F. Famà, J. Catani, A. Fioretti, C. Gabbanini, R. N. Bisset, L. Santos, and G. Modugno, Observation of a dipolar quantum gas with metastable supersolid properties, *Phys. Rev. Lett.* **122**, 130405 (2019).
- [10] F. Böttcher, J.-N. Schmidt, M. Wenzel, J. Hertkorn, M. Guo, T. Langen, and T. Pfau, Transient supersolid properties in an array of dipolar quantum droplets, *Phys. Rev. X* **9**, 011051 (2019).
- [11] L. Chomaz, D. Petter, P. Ilzhöfer, G. Natale, A. Trautmann, C. Politi, G. Durastante, R. M. W. van Bijnen, A. Patscheider, M. Sohmen, M. J. Mark, and F. Ferlaino, Long-lived and transient supersolid behaviors in dipolar quantum gases, *Phys. Rev. X* **9**, 021012 (2019).
- [12] M. Sohmen, C. Politi, L. Klaus, L. Chomaz, M. J. Mark, M. A. Norcia, and F. Ferlaino, Birth, life, and death of a dipolar supersolid, *Phys. Rev. Lett.* **126**, 233401 (2021).
- [13] T. Bland, E. Poli, C. Politi, L. Klaus, M. A. Norcia, F. Ferlaino, L. Santos, and R. N. Bisset, Two-dimensional supersolid formation in dipolar condensates, *Phys. Rev. Lett.* **128**, 195302 (2022).
- [14] S. M. Rocuzzo and F. Ancilotto, Supersolid behavior of a dipolar Bose-Einstein condensate confined in a tube, *Phys. Rev. A* **99**, 041601 (2019).
- [15] P. B. Blakie, D. Baillie, L. Chomaz, and F. Ferlaino, Supersolidity in an elongated dipolar condensate, *Phys. Rev. Res.* **2**, 043318 (2020).
- [16] J. C. Smith, D. Baillie, and P. B. Blakie, Supersolidity and crystallization of a dipolar Bose gas in an infinite tube, *Phys. Rev. A* **107**, 033301 (2023).
- [17] Y.-C. Zhang, F. Maucher, and T. Pohl, Supersolidity around a critical point in dipolar Bose-Einstein condensates, *Phys. Rev. Lett.* **123**, 015301 (2019).
- [18] Y.-C. Zhang, T. Pohl, and F. Maucher, Phases of supersolids in confined dipolar Bose-Einstein condensates, *Phys. Rev. A* **104**, 013310 (2021).
- [19] B. T. E. Ripley, D. Baillie, and P. B. Blakie, Two-dimensional supersolidity in a planar dipolar Bose gas, *Phys. Rev. A* **108**, 053321 (2023).
- [20] Y.-C. Zhang, T. Pohl, and F. Maucher, Metastable patterns in one- and two-component dipolar Bose-Einstein condensates, *Phys. Rev. Res.* **6**, 023023 (2024).
- [21] M. E. Fisher, Renormalization of critical exponents by hidden variables, *Phys. Rev.* **176**, 257 (1968).
- [22] G. Ódor, Universality classes in nonequilibrium lattice systems, *Rev. Mod. Phys.* **76**, 663 (2004).
- [23] J. Zinn-Justin, *Quantum field theory and critical phenomena*, 4th ed., International Series of Monographs on Physics (Clarendon Press, Oxford, England, 2002).
- [24] T. W. B. Kibble, Topology of cosmic domains and strings, *Journal of Physics A: Mathematical and General* **9**, 1387 (1976).
- [25] T. W. B. Kibble, Some implications of a cosmological phase transition, *Physics Reports* **67**, 183 (1980).
- [26] W. H. Zurek, Cosmological experiments in superfluid helium?, *Nature* **317**, 505 (1985).
- [27] W. H. Zurek, Cosmological experiments in condensed matter systems, *Physics Reports* **276**, 177 (1996).
- [28] A. del Campo and W. H. Zurek, Universality of phase transition dynamics: Topological defects from symmetry breaking, *Int. J. Mod. Phys. A* **29**, 1430018 (2014).
- [29] T. W. B. Kibble, Phase-transition dynamics in the lab and the universe, *Physics Today* **60**, 47 (2007).
- [30] W. H. Zurek, Causality in condensates: Gray solitons as relics of BEC formation, *Phys. Rev. Lett.* **102**, 105702 (2009).
- [31] B. Damski and W. H. Zurek, Soliton creation during a Bose-Einstein condensation, *Phys. Rev. Lett.* **104**, 160404 (2010).
- [32] A. del Campo, A. Retzker, and M. B. Plenio, The inhomogeneous Kibble-Zurek mechanism: vortex nucleation during Bose-Einstein condensation, *New Journal of Physics* **13**, 083022 (2011).
- [33] A. Das, J. Sabbatini, and W. H. Zurek, Winding up superfluid in a torus via Bose Einstein condensation, *Scientific Reports* **2**, 352 (2012).
- [34] A. del Campo, T. W. B. Kibble, and W. H. Zurek, Causality and non-equilibrium second-order phase transitions in inhomogeneous systems, *Journal of Physics: Condensed Matter* **25**, 404210 (2013).
- [35] S.-W. Su, S.-C. Gou, A. Bradley, O. Fialko, and J. Brand, Kibble-Zurek scaling and its breakdown for spontaneous generation of Josephson vortices in Bose-Einstein condensates, *Phys. Rev. Lett.* **110**, 215302 (2013).
- [36] J. Beugnon and N. Navon, Exploring the Kibble-Zurek mechanism with homogeneous Bose gases, *J. Phys. B: At.*

- Mol. Opt. Phys.* **50**, 022002 (2017).
- [37] S. Liu and Y. Zhang, Quench dynamics in a trapped Bose-Einstein condensate with spin-orbit coupling, *Phys. Rev. A* **99**, 053609 (2019).
- [38] P. Comaron, F. Larcher, F. Dalfovo, and N. P. Proukakis, Quench dynamics of an ultracold two-dimensional Bose gas, *Phys. Rev. A* **100**, 033618 (2019).
- [39] X. Jiang, S. Wu, Q. Ye, and C. Lee, Universality of miscible-immiscible phase separation dynamics in two-component Bose-Einstein condensates, *New Journal of Physics* **21**, 023014 (2019).
- [40] I.-K. Liu, J. Dziarmaga, S.-C. Gou, F. Dalfovo, and N. P. Proukakis, Kibble-Zurek dynamics in a trapped ultracold Bose gas, *Phys. Rev. Res.* **2**, 033183 (2020).
- [41] M. T. Wheeler, H. Salman, and M. O. Borgh, Dynamics of a nonequilibrium discontinuous quantum phase transition in a spinor Bose-Einstein condensate, arXiv:2312.16555 [cond-mat.stat-mech] [10.48550/ARXIV.2312.16555](https://arxiv.org/abs/2312.16555) (2023).
- [42] M. Thudiyangal and A. del Campo, Universal vortex statistics and stochastic geometry of Bose-Einstein condensation, *Phys. Rev. Res.* **6**, 033152 (2024).
- [43] N. P. Proukakis, Universality of Bose-Einstein condensation and quenched formation dynamics, in *Encyclopedia of Condensed Matter Physics* (Elsevier, 2024) pp. 84–123.
- [44] C. N. Weiler, T. W. Neely, D. R. Scherer, A. S. Bradley, M. J. Davis, and B. P. Anderson, Spontaneous vortices in the formation of Bose-Einstein condensates, *Nature* **455**, 948 (2008).
- [45] G. Lamporesi, S. Donadello, S. Serafini, F. Dalfovo, and G. Ferrari, Spontaneous creation of Kibble-Zurek solitons in a Bose-Einstein condensate, *Nature Physics* **9**, 656 (2013).
- [46] L. Corman, L. Chomaz, T. Bienaimé, R. Desbuquois, C. Weitenberg, S. Nascimbène, J. Dalibard, and J. Beugnon, Quench-induced supercurrents in an annular Bose gas, *Phys. Rev. Lett.* **113**, 135302 (2014).
- [47] N. Navon, A. L. Gaunt, R. P. Smith, and Z. Hadzibabic, Critical dynamics of spontaneous symmetry breaking in a homogeneous Bose gas, *Science* **347**, 167 (2015).
- [48] L. Chomaz, L. Corman, T. Bienaimé, R. Desbuquois, C. Weitenberg, S. Nascimbène, J. Beugnon, and J. Dalibard, Emergence of coherence via transverse condensation in a uniform quasi-two-dimensional Bose gas, *Nature Communications* **6**, 6162 (2015).
- [49] S. Donadello, S. Serafini, T. Bienaimé, F. Dalfovo, G. Lamporesi, and G. Ferrari, Creation and counting of defects in a temperature-quenched Bose-Einstein condensate, *Phys. Rev. A* **94**, 023628 (2016).
- [50] L. W. Clark, L. Feng, and C. Chin, Universal space-time scaling symmetry in the dynamics of bosons across a quantum phase transition, *Science* **354**, 606 (2016).
- [51] I. K. Liu, S. Donadello, G. Lamporesi, G. Ferrari, S. C. Gou, F. Dalfovo, and N. P. Proukakis, Dynamical equilibration across a quenched phase transition in a trapped quantum gas, *Communications Physics* **1**, 24 (2018).
- [52] B. Ko, J. W. Park, and Y. Shin, Kibble-Zurek universality in a strongly interacting Fermi superfluid, *Nature Physics* **15**, 1227 (2019).
- [53] J. Goo, Y. Lim, and Y. Shin, Defect saturation in a rapidly quenched Bose gas, *Phys. Rev. Lett.* **127**, 115701 (2021).
- [54] X.-P. Liu, X.-C. Yao, Y. Deng, Y.-X. Wang, X.-Q. Wang, X. Li, Q. Chen, Y.-A. Chen, and J.-W. Pan, Dynamic formation of quasicondensate and spontaneous vortices in a strongly interacting Fermi gas, *Phys. Rev. Res.* **3**, 043115 (2021).
- [55] J. Goo, Y. Lee, Y. Lim, D. Bae, T. Rabga, and Y. Shin, Universal early coarsening of quenched Bose gases, *Phys. Rev. Lett.* **128**, 135701 (2022).
- [56] T. Rabga, Y. Lee, D. Bae, M. Kim, and Y. Shin, Variations of the Kibble-Zurek scaling exponents of trapped Bose gases, *Phys. Rev. A* **108**, 023315 (2023).
- [57] D. G. Allman, P. Sabharwal, and K. C. Wright, Quench-induced spontaneous currents in rings of ultracold fermionic atoms, *Phys. Rev. A* **109**, 053320 (2024).
- [58] L. E. Sadler, J. M. Higbie, S. R. Leslie, M. Vengalattore, and D. M. Stamper-Kurn, Spontaneous symmetry breaking in a quenched ferromagnetic spinor Bose-Einstein condensate, *Nature* **443**, 312 (2006).
- [59] D. Chen, M. White, C. Borries, and B. DeMarco, Quantum quench of an atomic mott insulator, *Phys. Rev. Lett.* **106**, 235304 (2011).
- [60] M. Anquez, B. A. Robbins, H. M. Bharath, M. Boguslawski, T. M. Hoang, and M. S. Chapman, Quantum Kibble-Zurek mechanism in a spin-1 Bose-Einstein condensate, *Phys. Rev. Lett.* **116**, 155301 (2016).
- [61] L. Feng, L. W. Clark, A. Gaj, and C. Chin, Coherent inflationary dynamics for Bose-Einstein condensates crossing a quantum critical point, *Nature Physics* **14**, 269 (2017).
- [62] Y. Chen, M. Horikoshi, K. Yoshioka, and M. Kuwata-Gonokami, Dynamical critical behavior of an attractive Bose-Einstein condensate phase transition, *Phys. Rev. Lett.* **122**, 040406 (2019).
- [63] C.-R. Yi, S. Liu, R.-H. Jiao, J.-Y. Zhang, Y.-S. Zhang, and S. Chen, Exploring inhomogeneous Kibble-Zurek mechanism in a spin-orbit coupled Bose-Einstein condensate, *Phys. Rev. Lett.* **125**, 260603 (2020).
- [64] K. Lee, S. Kim, T. Kim, and Y. Shin, Universal Kibble-Zurek scaling in an atomic Fermi superfluid, *Nature Physics* **20**, 1570 (2024).
- [65] I. Ferrier-Barbut, H. Kadau, M. Schmitt, M. Wenzel, and T. Pfau, Observation of quantum droplets in a strongly dipolar Bose gas, *Phys. Rev. Lett.* **116**, 215301 (2016).
- [66] F. Wächtler and L. Santos, Quantum filaments in dipolar Bose-Einstein condensates, *Phys. Rev. A* **93**, 061603 (2016).
- [67] L. Chomaz, S. Baier, D. Petter, M. J. Mark, F. Wächtler, L. Santos, and F. Ferlaino, Quantum-fluctuation-driven crossover from a dilute Bose-Einstein condensate to a macrodroplet in a dipolar quantum fluid, *Phys. Rev. X* **6**, 041039 (2016).
- [68] A. R. P. Lima and A. Pelster, Quantum fluctuations in dipolar Bose gases, *Phys. Rev. A* **84**, 041604 (2011).
- [69] P. B. Blakie, D. Baillie, and S. Pal, Variational theory for the ground state and collective excitations of an elongated dipolar condensate, *Communications in Theoretical Physics* **72**, 085501 (2020).
- [70] S. Pal, D. Baillie, and P. B. Blakie, Excitations and number fluctuations in an elongated dipolar Bose-Einstein condensate, *Phys. Rev. A* **102**, 043306 (2020).
- [71] P. B. Blakie, L. Chomaz, D. Baillie, and F. Ferlaino, Compressibility and speeds of sound across the superfluid-to-supersolid phase transition of an elongated dipolar gas, *Phys. Rev. Res.* **5**, 033161 (2023).
- [72] See Supplemental Material at [URL\\_will\\_be\\_inserted\\_by\\_publisher](https://www.nature.com/articles/s41534-024-01039-1) for details on the initial thermal and quan-

- tum noise, comparison of results to full 3D calculations, verification of results against system size, and an outline for how the quantities  $g^{(2)}(x)$  and  $C(x)$  are related.
- [73] We therefore suggest that care must be taken when using a function like  $C(x)$  to determine KZM scaling results, especially at quench rates where  $\xi$  begins to approach  $L_{uc}$ , and perhaps greater statistics are needed for proper convergence of this measure.
- [74] H.-B. Zeng, C.-Y. Xia, and A. del Campo, Universal breakdown of Kibble-Zurek scaling in fast quenches across a phase transition, *Phys. Rev. Lett.* **130**, 060402 (2023).
- [75] S. Sachdev, *Quantum Phase Transitions*, 2nd ed. (Cambridge University Press, 2011).
- [76] P. C. Hohenberg and B. I. Halperin, Theory of dynamic critical phenomena, *Rev. Mod. Phys.* **49**, 435 (1977).
- [77] A. Jelić and L. F. Cugliandolo, Quench dynamics of the 2dxymodel, *Journal of Statistical Mechanics: Theory and Experiment* **2011**, P02032 (2011).
- [78] J. Dziarmaga and W. H. Zurek, Quench in the 1d Bose-Hubbard model: Topological defects and excitations from the Kosterlitz-Thouless phase transition dynamics, *Scientific Reports* **4**, 5950 (2014).
- [79] B. Gardas, J. Dziarmaga, and W. H. Zurek, Dynamics of the quantum phase transition in the one-dimensional Bose-Hubbard model: Excitations and correlations induced by a quench, *Phys. Rev. B* **95**, 104306 (2017).
- [80] Z. Zuo, S. Yin, X. Cao, and F. Zhong, Scaling theory of the Kosterlitz-Thouless phase transition, *Phys. Rev. B* **104**, 214108 (2021).
- [81] M. P. A. Fisher, P. B. Weichman, G. Grinstein, and D. S. Fisher, Boson localization and the superfluid-insulator transition, *Phys. Rev. B* **40**, 546 (1989).
- [82] Q. Huang, R. Yao, L. Liang, S. Wang, Q. Zheng, D. Li, W. Xiong, X. Zhou, W. Chen, X. Chen, and J. Hu, Observation of many-body quantum phase transitions beyond the Kibble-Zurek mechanism, *Phys. Rev. Lett.* **127**, 200601 (2021).
- [83] A. van Otterlo, K.-H. Wagenblast, R. Baltin, C. Bruder, R. Fazio, and G. Schön, Quantum phase transitions of interacting bosons and the supersolid phase, *Phys. Rev. B* **52**, 16176 (1995).
- [84] F. Bloch, Superfluidity in a ring, *Phys. Rev. A* **7**, 2187 (1973).
- [85] C. Ryu, M. F. Andersen, P. Cladé, V. Natarajan, K. Helmerson, and W. D. Phillips, Observation of persistent flow of a Bose-Einstein condensate in a toroidal trap, *Phys. Rev. Lett.* **99**, 260401 (2007).
- [86] A. Ramanathan, K. C. Wright, S. R. Muniz, M. Zelan, W. T. Hill, C. J. Lobb, K. Helmerson, W. D. Phillips, and G. K. Campbell, Superflow in a toroidal Bose-Einstein condensate: An atom circuit with a tunable weak link, *Phys. Rev. Lett.* **106**, 130401 (2011).
- [87] K. C. Wright, R. B. Blakestad, C. J. Lobb, W. D. Phillips, and G. K. Campbell, Driving phase slips in a superfluid atom circuit with a rotating weak link, *Phys. Rev. Lett.* **110**, 025302 (2013).
- [88] S. Eckel, J. G. Lee, F. Jendrzejewski, N. Murray, C. W. Clark, C. J. Lobb, W. D. Phillips, M. Edwards, and G. K. Campbell, Hysteresis in a quantized superfluid ‘atomic’ circuit, *Nature* **506**, 200 (2014).
- [89] K. Henderson, C. Ryu, C. MacCormick, and M. G. Boshier, Experimental demonstration of painting arbitrary and dynamic potentials for Bose-Einstein condensates, *New J. Phys.* **11**, 043030 (2009).
- [90] B. E. Sherlock, M. Gildemeister, E. Owen, E. Nugent, and C. J. Foot, Time-averaged adiabatic ring potential for ultracold atoms, *Phys. Rev. A* **83**, 043408 (2011).
- [91] S. Moulder, S. Beattie, R. P. Smith, N. Tammuz, and Z. Hadzibabic, Quantized supercurrent decay in an annular Bose-Einstein condensate, *Phys. Rev. A* **86**, 013629 (2012).
- [92] C. Ryu, P. W. Blackburn, A. A. Blinova, and M. G. Boshier, Experimental realization of Josephson junctions for an atom squid, *Phys. Rev. Lett.* **111**, 205301 (2013).
- [93] S. Beattie, S. Moulder, R. J. Fletcher, and Z. Hadzibabic, Persistent currents in spinor condensates, *Phys. Rev. Lett.* **110**, 025301 (2013).
- [94] G. E. Marti, R. Olf, and D. M. Stamper-Kurn, Collective excitation interferometry with a toroidal Bose-Einstein condensate, *Phys. Rev. A* **91**, 013602 (2015).
- [95] M. Nilsson Tengstrand, D. Bohlm, R. Sachdeva, J. Bengtsson, and S. M. Reimann, Persistent currents in toroidal dipolar supersolids, *Phys. Rev. A* **103**, 013313 (2021).
- [96] M. Nilsson Tengstrand, P. Stürmer, J. Ribbing, and S. M. Reimann, Toroidal dipolar supersolid with a rotating weak link, *Phys. Rev. A* **107**, 063316 (2023).